

# Biowaste-Derived Carbonized Bone for Solar Steam Generation and Seawater Desalination

Muhammad Shajih Zafar, Muhammad Zahid, Athanassia Athanassiou, and Despina Fragouli\*

Interfacial solar steam generation is an emerging strategy to improve the global freshwater supply. Herein, for the first time, a plausible alternative based on bone waste is presented for low-cost solar steam generation and seawater desalination. This is accomplished via the exploration of the appropriate carbonization conditions for the successful bone transformation into a porous carbon-based photothermal material. The carbonized bone (CB) not only is composed of inherent interlinked mesoporous microchannels for efficient water transportation but also displays broadband light absorption, photothermal conversion, and reduced vaporization enthalpy due to its special interactions with water. The as-prepared CB shows an apparent evaporation rate of  $1.82 \text{ kg m}^{-2} \text{ h}^{-1}$  under one-sun illumination, attributed not only to its interaction with the sunlight but also to its performance in the dark field, and a solar-to-vapor conversion efficiency of 80%. Furthermore, CB desalinates water with an efficiency of 99.99%. Such performance combined with its wide availability, facile fabrication, and stability makes this biowaste-based porous material a promising system for the production of freshwater. In this way, a valuable alternative for the valorization of bone-based food-waste is offered, paving the way to new routes for the management of such, continuously growing, food-waste products.

produce potable water,<sup>[2]</sup> to substitute the current technologies. The available technologies require large centralized infrastructure and high energy consumption limiting their applicability especially in the offshore areas, small villages, or remote off-grid regions.<sup>[3]</sup>

A valuable alternative for an effective, low-cost, and easy to implement technology for potable water production has been recently demonstrated to be solar steam generation.<sup>[4]</sup> In this process, solar energy is exploited to generate steam from the water through a photothermal process, by using diverse porous materials based on plasmonic,<sup>[5]</sup> semiconductors,<sup>[6]</sup> and carbon-based systems,<sup>[7–9]</sup> which are able to absorb solar light and efficiently transform it into heat.<sup>[5,7]</sup>

Carbon-based materials such as graphene, carbon nanotubes, or nanofibers are widely used as components of porous materials for a solar steam generation because of their broad light absorption,

good stability, and large surface area.<sup>[10,11]</sup> Nevertheless, these materials are typically expensive, their fabrication involves noxious chemicals (e.g., the liquid-phase exfoliation process), and their production and handling present diverse difficulties.<sup>[10,11]</sup> Alternatively, biobased,<sup>[9,12–19]</sup> and food-waste<sup>[16,20–22]</sup> carbonized materials have been successfully prepared following straightforward methods, resulting in cost-effective materials with favorable properties for an ideal photothermal system. In fact, they possess an outstanding ability of light absorption, highly porous structure and hydrophilicity, and good photothermal properties, all essential for efficient solar-driven steam production.<sup>[12,13]</sup> Therefore, due to their inherent properties, biowaste materials have a huge potential to be successfully used in this application and their further processing and exploration are continuously growing.<sup>[23]</sup> In fact, apart from their favorable properties, carbonized biobased materials are economical and are available in great abundance, making this approach an optimal sustainable solution to counter the forthcoming water shortage problem.


Animal bone is categorized among the most abundant biowaste materials. According to a recent report, the global meat industry produces 130 billion kg of animal bone per annum with over 10% produced in the European Union.<sup>[24]</sup> The animal bone's composition is a valuable source for the development of diverse materials for advanced applications. Specifically, bone is

## 1. Introduction

In the last few decades, freshwater resources have been significantly limited and, as reported by the Global Sustainable Development Report of the United Nations,<sup>[1]</sup> by 2025 two-thirds of the world population will be living in water-stressed conditions. Therefore, it is essential to develop and adopt efficient ways to

M. S. Zafar, Dr. M. Zahid, Dr. A. Athanassiou, Dr. D. Fragouli  
 Smart Materials Group  
 Istituto Italiano di Tecnologia  
 via Morego 30, Genova 16163, Italy  
 E-mail: despina.fragouli@iit.it

M. S. Zafar  
 Dipartimento di Informatica, Bioingegneria, Robotica e Ingegneria dei Sistemi (DIBRIS)  
 Università degli Studi di Genova  
 Via Opera Pia 13, Genova 16145, Italy

 The ORCID identification number(s) for the author(s) of this article can be found under <https://doi.org/10.1002/adsu.202100031>.

© 2021 The Authors. Advanced Sustainable Systems published by Wiley-VCH GmbH. This is an open access article under the terms of the Creative Commons Attribution License, which permits use, distribution and reproduction in any medium, provided the original work is properly cited.

DOI: 10.1002/adsu.202100031

an organic–inorganic composite that contains 22–45% collagen and 50–74% hydroxyapatite (HA) by weight,<sup>[25]</sup> and, apart from its most frequent use as a precursor for the preparation of high-defect and low-cost porous carbon materials,<sup>[26]</sup> many efforts have been devoted for the exploitation of new ways of transformation into advanced products for innovative applications such as supercapacitor electrodes for energy storage devices,<sup>[27,28]</sup> oxygen reduction reaction materials for fuel cells,<sup>[29]</sup> and adsorbents for fluoride removal from contaminated water.<sup>[30]</sup> Although bone presents essential features for photothermal water evaporation applications such as a highly porous interconnected structure, structural integrity, and appropriate hydrophilicity, to the best of our knowledge, no reports have been presented yet for its processing and utilization in solar steam generation and seawater desalination.

In this work, cattle bone waste has been thermally treated, to realize solar steam generators, and the effect of the temperature treatment on the performance of the carbonized bone (CB), following detailed physicochemical characterizations is investigated. We prove that the capability of an efficient solar steam generation is attributed to the unique hierarchical porous structure of the CB, which includes interconnected mesoporous microchannels in the bulk, combined with its broadband light absorption in the whole solar spectrum, its special interactions with water which result in reduced vaporization enthalpy, as well as with the advanced photothermal performance, resulting in a high evaporation rate and solar-to-vapor conversion efficiency. Most importantly with this sustainable material, it was possible to collect freshwater from artificial seawater with a desalination efficiency of 99.99%. As such, these findings pave the way for the valorization of the bone biowaste and the development of bioderived high-performance devices for solar steam-generation and the production of clean water.

## 2. Results and Discussion

To prepare the photothermal material, cattle bone waste after boiling in water for 15 min was sectioned transversally into a thin slice (Figure S1a, Supporting Information). The pristine bone slices were directly carbonized under nitrogen atmosphere at different temperatures (400, 600, and 800 °C) and their color changes from whitish to black in all cases (Figure S1b,c, Supporting Information). Hereafter, the bone samples carbonized at 400, 600, and 800 °C are named CB400, CB600, and CB800, respectively.

Generally, bones consist of mineralized fibrous organic-based tissue, with a hierarchical organization, which forms a system of longitudinal (Haversian) canals connected by transverse (Volkmann's) canals.<sup>[31]</sup> In particular, narrow and long crystalline units of collagen molecules are wrapped by proteins, forming nanofibrils. Collagen nanofibril clusters are arranged in parallel to form long collagen-based fibers, while the spacing among the fiber clusters is filled up with biominerals, mostly HA nanocrystals. Generally, after thermal treatment in a nitrogen atmosphere, the mineralized fibers are carbonized resulting in the formation of carbon-HA based fibrils, with their morphology and configuration preserved, as also the whole porous skeleton of the bone.<sup>[28]</sup>

To confirm and further evaluate the overall bone structure after the carbonization process, the scanning electron microscope (SEM) images of the pristine and CB samples were acquired (Figure 1 and Figures S2 and S3, Supporting Information). Before the carbonization, the pristine bone merely shows an inner porous structure (Figure S2, Supporting Information). In particular, the pristine bone slice appears compact because the pores are filled with organic compounds (e.g., protein, lipids, etc.) and entrapped water.<sup>[27]</sup> However, after carbonization a porous structure consisting of a fibrous texture and highly interlinked longitudinal and transversal microchannels is revealed. In particular, the cross-section SEM images of the CB400, CB600, and CB800 (Figure 1a–f) show the presence of longitudinal microchannels characteristic of the Haversian canals, that run throughout the bulk bone structure along its axis, and of transversal pores.<sup>[31]</sup> As the carbonization temperature increases, the surface morphology of the microchannel walls becomes more rough and at the same time, the presence of a fibrillar texture, consisting of fibers with diameter ranging mostly between 0.04 and 0.12 μm (Figure S4, Supporting Information) is revealed (insets of Figure 1b,d,f). The fiber bundles are intertwined along the longitudinal axis of the canals and small holes are present between the bundles, leaving spaces for osteocyte canaliculi<sup>[31]</sup> (indicated by the white arrows at the insets for Figure 1). This texture and configuration are characteristic of the collagen fibers densely packed together proving that the carbonization process does not alter the morphology of the natural bone structure. Overall, the SEM imaging of the CBs displays a fibrous structure with an intense network of interconnected microchannels and pores typical of a compact bone.<sup>[31]</sup>

In order to evaluate the porous structure, combined pore size distribution analysis of the SEM images, mercury intrusion porosimetry (MIP), and Brunauer–Emmett–Teller (BET) studies are performed. The size distribution analysis of the microchannels using the SEM images (Figure S5, Supporting Information) reveals that the longitudinal microchannels (Haversian canals) have diameters in the range of ≈10–70 μm while the transversal pores have two different size ranges of few micrometers and few tens of micrometers (blue and red arrows respectively at Figure 1), independently on the adopted heat-treatment process. The interlinked pores were further characterized using MIP that demonstrates that all CBs present a bimodal porous structure in two different size ranges of ≈0.008–0.5 and ≈3–50 μm (Section S13 and Figure S6, Supporting Information). The larger pores (3–50 μm) correspond to Haversian and Volkmann's canals as also proved by the analysis of the SEM images while the pores in the smaller range can be attributed to the osteocyte lacunar spaces and the interconnected network of canaliculi that enables the communication within the bone matrix.<sup>[32]</sup> It should be noted that the presence of pores with a diameter in the range between 4 and 20 μm is significantly evident in the case of CB600 compared to the CB400 and CB800. The presence of higher amount of pores in such size range may contribute to the enhancement of the bulk porosity. In fact, MIP and the real density analyses (Section S13 and Table S1, Supporting Information) confirm that CB600 has a higher effective porosity (48.6%) compared to the CB400 (41.3%) indicating that the treatment at 600 °C

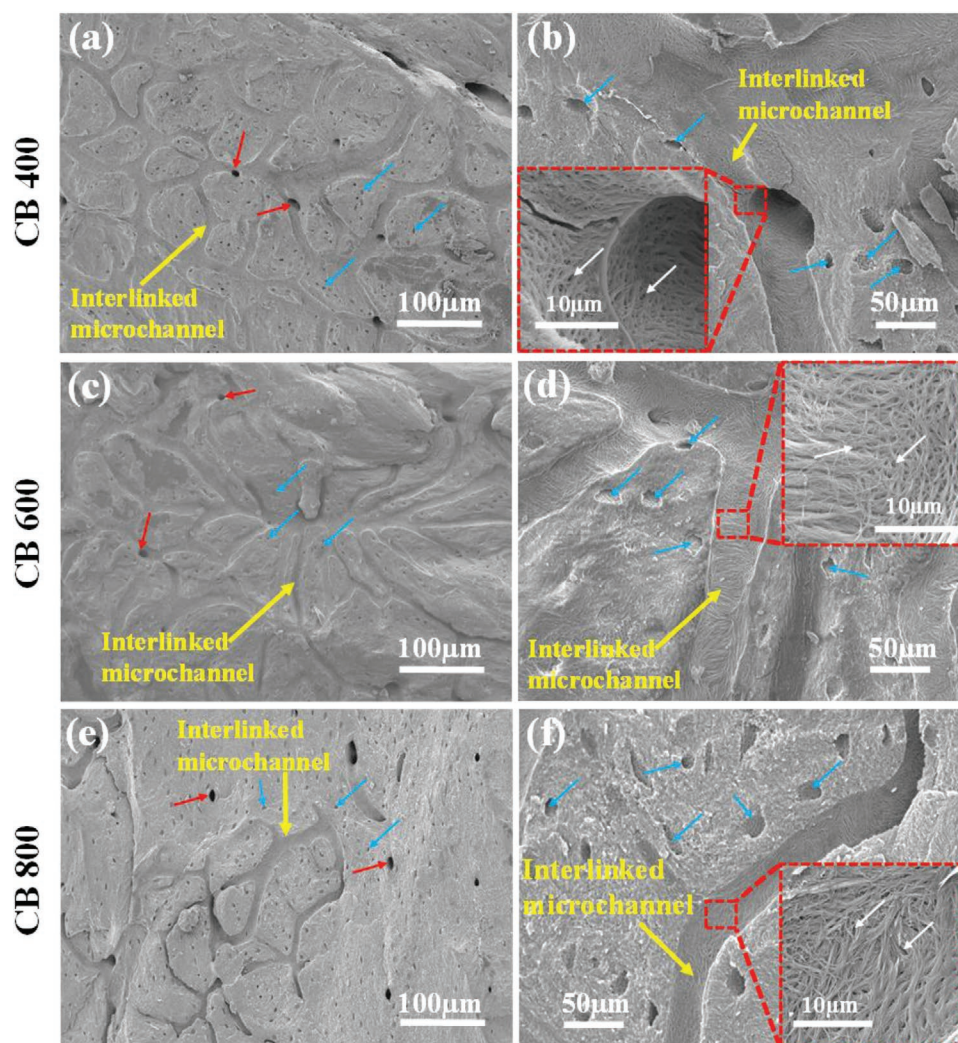


**Figure 1.** Cross-sectional SEM images of the CBs at different magnifications, showing the interlinked microchannels combined with fibrous-like structure and smaller pores of a,b) CB400, c,d) CB600, and e,f) CB800. Insets: Surface morphology of the microchannels at higher magnification. Arrows indicate the different types of pores present.

efficiently removes the organic substances from the pores. On the other hand treatment at 800 °C causes a decrease in the porosity (45.8%), in accordance with previous studies,<sup>[32,33]</sup> indicating that the HA-based bone structure starts being affected as the temperature of the thermal treatment increases.<sup>[32,33]</sup>

To better investigate the structure of the CBs in the mesopore range, the BET analysis is also performed. As shown in Section S14 in the Supporting Information, mesopores in the range from 3 to 20 nm are present in all CBs. Similar mesopore distribution is also observed at the pristine bone and this reveals that this type of pores can be attributed to the empty spaces between collagen fibers and the HA crystals.<sup>[32]</sup> Although the mesopore size distribution is not altered significantly upon heat treatment, the cumulative pore volume increases from 0.215 for the pristine bone to 0.319 cc g<sup>-1</sup> for the CB800. The specific surface area also increases from 122.7 for the fresh bone to 136.4 m<sup>2</sup> g<sup>-1</sup> for the CB800 (Figure S7 and Table S2, Supporting Information). These facts indicate that the thermal processing induces the unclogging of the mesopores from the humidity and the organic components.

The study of the decomposition of the pristine bone during the thermal treatment and the evaluation of the composition of the CBs were performed by the thermogravimetric analysis (TGA) as shown in **Figure 2**. For the pristine bone (Figure 2a), the TGA curve shows a continuous weight decrease from 30 to 800 °C, which represents a ≈33.8% loss of its total mass. This occurs in three well-defined steps. At the first step up to 150 °C, a weight loss of ≈9.1% occurs and can be attributed to the release of adsorbed moisture. At the second step, the weight loss is about 18.8% and the maximum rate occurs at 330 °C (Figure 2b), due to the thermolysis of the organic matter (fat and proteins),<sup>[34]</sup> while the third degradation step starts at temperatures higher than 650 °C with a weight loss of ≈5.9% at 800 °C, related to the thermolysis of carbonates and the partial dehydroxylation of HA.<sup>[34–37]</sup> On the other hand, for the CBs, less decomposition steps and smaller weight losses are observed. Specifically, in all cases the first step up to 150 °C is attributed to the release of adsorbed moisture and measures ≈4.5, ≈5.3, and ≈3.3% for CB400, CB600, and CB800, respectively. When

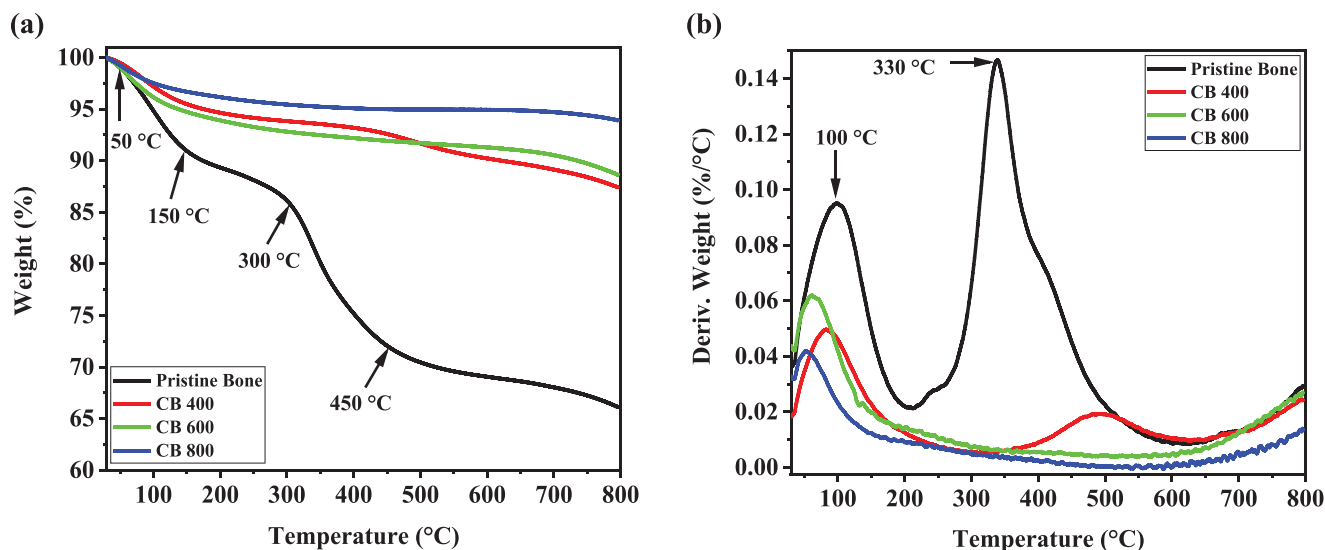


**Figure 2.** a) TGA and b) differential thermogravimetry of the pristine bone and the CBs in  $N_2$  atmosphere.

the bone is carbonized at the lowest temperature, CB400, a second degradation step is observed at 350–600 °C due to the decomposition of the remaining organic residuals, and a third slower step starting from 650 °C onward is due to the decomposition of carbonates and the partial dehydroxylation of hydroxyapatite,<sup>[34–37]</sup> (total weight loss  $\approx 12.1\%$  from 30 to 800 °C). Differently, the CB600 demonstrates solely the decomposition step starting from 650 °C while the decomposition step of the CB800 starts only close to 800 °C. These steps are attributed to the decomposition of carbonates and the partial dehydroxylation of HA (at a temperature higher than 800 °C), with total weight losses of  $\approx 10.5\%$  and  $\approx 5.3\%$  at 800 °C, respectively. This proves the successful removal of the organic components during their fabrication process of the CB600 and CB800, in contrast to the CB400 which is partially carbonized.

To further explore the chemical composition of the samples, the Fourier transform infrared spectroscopy (FTIR) analysis is performed (see **Figure 3a**). For the pristine bone, the broad peaks at 3281 and 1642  $cm^{-1}$  are associated with the stretching vibration of O–H due to adsorbed moisture.<sup>[37]</sup> The latter can also be attributed to the O–H group of HA.<sup>[38]</sup> The bands associated with the amide-II groups of proteins (i.e., organic materials) are detected at 1240 and 1541  $cm^{-1}$ ,<sup>[39]</sup> and their weak contribution to the overall spectrum can be attributed to the partial denaturation and leakage of the proteins by the boiling pretreatment process.<sup>[40]</sup> Two other peaks are also attributed to the presence of organic materials present in the bone and are the symmetric and asymmetric stretching vibrations of the C–H bond which appear at 2853 and 2922  $cm^{-1}$ .<sup>[41]</sup> On the other hand, the bands at 872, 1414, and 1456  $cm^{-1}$  are related to the stretching vibrations of the carbonate group ( $CO_3^{2-}$ ), while the dominant band at 1007  $cm^{-1}$  and the band at 962  $cm^{-1}$  are related to the stretching vibration of the phosphate group,<sup>[42]</sup> both components of the HA ( $Ca_x(PO_4)_y(OH)_z$ ). After the carbonization process, for all CBs, the peaks attributed to the carbonate and phosphate groups (1456, 1414, 1007, 961, and 872  $cm^{-1}$ ) do not change confirming the presence of the HA. However, the presence of the bands associated with

the symmetric and asymmetric C–H vibrations at 2853 and 2922  $cm^{-1}$  is significantly attenuated in the CB400 (**Figure 3b**) and eventually, the bands disappear in the CB600 and CB800. It is worth noting that the evaluation of the evolution of the amide-II groups was not possible using the FTIR spectra due to the reduced intensity of these bands. However, an estimation was performed by X-ray photoelectron spectroscopy (XPS) analysis, as the presence of N in the survey spectra suggests the presence of organic compounds in the bone. As shown in **Figure S8** and **Table S3** in the Supporting Information, the N element is present in trace amounts only in the pristine bone and at the CB400, further confirming the successful carbonization process and the removal of the organic compounds in the CB600 and CB800. Finally, the broad band at 3281  $cm^{-1}$  related to the adsorbed humidity, becomes less intense at the CBs in agreement with the TGA analysis, while the band at 1642  $cm^{-1}$  does not significantly change confirming the presence of the HA component in all cases. It should be mentioned that the peaks at 700 and 1014  $cm^{-1}$  present in the spectrum of the CB800 may be attributed to the N–C–N deformation and stretching modes of the cyanamide species, formed during the combustion of the nitrogen containing compounds of the bone structure.<sup>[43]</sup>

The CBs were also studied with Raman spectroscopy to evaluate the type of carbon they are composed of (**Figure 3c**). For all cases the strong vibrations of the C–C of the carbonaceous material are indicated by two intense peaks at 1356 and 1590  $cm^{-1}$ , attributed to the amorphous carbon ( $I_D$ ) that is characteristic of  $sp^3$  defects (i.e., defects) and graphite structure ( $I_G$ ) ( $sp^2$  bonded graphitic carbons), respectively.<sup>[44,45]</sup> As the temperature of the treatment increases, the  $I_G/I_D$  ratio, which indicates the degree of graphitization, increases. Specifically for CB400 is 0.93, while for CB600 and CB800, the values are 1.05 and 1.18 respectively.

**Figure 3d** shows the X-ray diffraction (XRD) spectra of the pristine bone and the CBs. All peaks observed are attributed to the characteristic peaks of standard HA (reference card (ICDD-01-074-9761)).<sup>[37]</sup> However, the diffraction peaks of the pristine

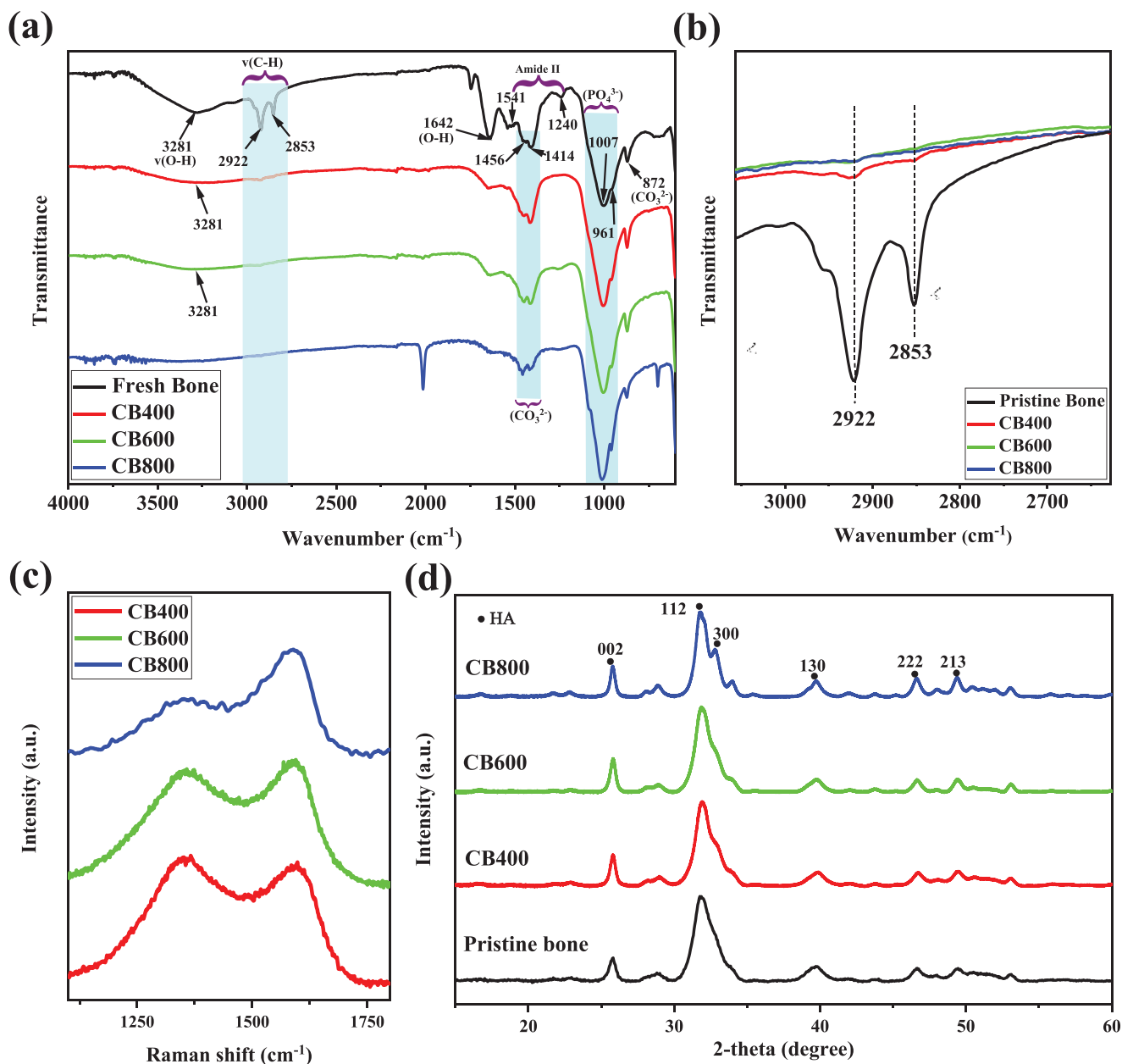


**Figure 3.** a) FTIR spectra of the pristine bone and the CBs. b) Zoom-in of the FTIR spectra in the region of the symmetric and asymmetric vibration peaks of the C–H group. c) Raman spectra of CBs and d) XRD analyses of the pristine bone and CBs.

bone appear somehow broader and less defined, compared to the peaks of the CBs, possibly ascribed to the existence of fibrous collagen in the sample which might lead to undesired scattering of the X-ray radiations.<sup>[37]</sup> The more defined and sharp peaks of the CB spectra, more obvious with the increase of the carbonization temperature, indicate that the crystallinity of the samples increases, as the carbonization process causes the elimination of the organic components without affecting the HA structure.<sup>[46]</sup>

The carbonization temperatures also affect the final wetting properties of the resulting materials, an important parameter for the steam-generation systems.<sup>[13]</sup> The surface wettability analysis of the CBs demonstrates that although all of them are

water absorbing, immediately after the droplet deposition on their surface, the water contact angles (WCAs) are  $57.0^\circ \pm 1.3^\circ$  for the CB400 and  $69.5^\circ \pm 1.7^\circ$  for the CB800. After few seconds, the droplets are absorbed by the porous samples (Figure S10, Supporting Information). In contrast, for the CB600, the droplet is immediately absorbed, showing its super wetting properties. In general, the surface wettability is governed by the functional groups present on the surface of a material and of its surface roughness and morphology.<sup>[47]</sup> As so far proved by the structural and chemical analysis of the samples, the CB400 presents various organic residues on its surface and bulk (XPS study presented at Figures S8 and S9 and Tables S3 and S4, Supporting Information) clogging the porous structure, and

therefore delaying the penetration of the water in its skeleton. On the other hand, the high carbonization temperature employed to prepare the CB800 results in the presence of more C–C components and a low amount of oxygenated moieties on its surface (Figure S9 and Table S4, Supporting Information). In fact, the rise in aliphatic carbon (i.e., C–C) and the reduced amount of oxygen, depicts that the hydrophilicity starts to decline,<sup>[48]</sup> and ultimately, this may affect the material's performance as a solar steam generator.

Therefore, it was decided to focus on the CB600 in order to explore its utilization as a steam-generation device. Before doing so, the interaction between the absorbed water and the hydrophilic CB600 was studied by differential scanning calorimetry (DSC) (Figure S11, Supporting Information). In general, the water may be present in three different states in hydrophilic materials: nonfreezable bound water which does not crystallize even at very low temperatures, freezable bound water which crystallizes at a temperature lower than 0 °C, and free water which crystallizes at 0 °C.<sup>[49]</sup> This behavior of the absorbed water can be attributed to various effects such as the capillary condensation, the strong interactions of the water molecules with the polar groups of the solid surface either directly or via other water molecules, etc.<sup>[50]</sup> From the DSC analysis, it is shown that the freezable water in the CB600 is present both as free and as bound water. In particular, by wetting the sample with water it can be seen the presence of two crystallization peaks. The peak observed at ≈5 °C, can be attributed to the freezable bound water and the peak at ≈0 °C is attributed to the bulk-free water, with the contribution of each state to depend on the volume of water used for the wetting. When the sample is wetted with a very low amount of water (1 μL) all the water molecules are interacting with the solid surface and therefore a single peak at –4.2 °C is observed. When a higher quantity of water is used (3 μL), a sharp peak associated with the bulk-free water appears, in addition to the wider peak of bound water at ≈5.0 °C, and their corresponding contributions to the overall amount of water are 43.87% and 56.13% respectively. Further increase of the water volume (5 μL) induced the higher contribution of the free water (66.33%) compared to the bound water (33.57%). Higher water quantities in the sample would result in the progressive merging of the two peaks into a broad one close to 0 °C,<sup>[49]</sup> indicating the prevalent contribution of the free water in the sample. The presence of freezable bound water states is very important for an efficient water evaporation performance, as it is required less energy to break the hydrogen bonds between the water molecules compared to the free water, facilitating, thus, the liquid-to-vapor phase change.<sup>[51]</sup> In fact, a molecule of free water interacts with four adjacent water molecules through hydrogen bonding forming stable configurations and therefore bulk water presents high vaporization enthalpy. On the other hand, the polar functional groups of a surface may capture water molecules by hydrogen bonds that are stronger than those between free-water molecules, generating bound (nonfreezable) water. Water molecules next to such bound-water molecules interact with fewer than four water molecules, forming intermediate (freezable) water which has weaker interactions with the adjacent water molecules, and therefore lower vaporization enthalpy.<sup>[52]</sup>

For a good steam generation performance, the porous samples must also exhibit good light absorption properties in

the entire solar spectrum. To characterize the photoabsorption ability of the CB600, absorption spectra were obtained in the wide range of 250–2500 nm as shown in Figure 4a. The samples show high absorption in the whole spectral range (90.0–99.3%) suggesting a very efficient absorption of the sun's radiance. This optical feature can be associated with the nature and color of the CB, and with its surface morphology and porous structure which may play a crucial role in the enhancement of the light-trapping from multiple light scattering.<sup>[53,54]</sup> It should be mentioned that the absorption of the CB400 and CB800 is similar to the one of the CB600 (Figure S12, Supporting Information).

For the practical evaluation of the light-to-heat conversion ability of the CB600, the surface temperature increase was estimated under one sun illumination using a thermal camera. Under exposure for 18 min, the temperature of the dry sample increases reaching 35.8 °C, while the CB400 and CB800 reached ≈31.7 and ≈30.0 °C respectively, proving that the CB600 interacts better with the light transforming it into heat more efficiently.

When the CB600 was brought into contact with the water (thermal conductivity in the wet state  $1.161 \pm 0.024 \text{ W m}^{-1} \text{ K}^{-1}$ , Figure S13, Supporting Information) using a polystyrene (PS) foam ring as support to float on the water surface, the temperature was increased on its surface upon light irradiation (Figure 4b). This is clearly demonstrated in Figure 4c, where the corresponding infrared (IR) images of the top surface of the CB600 floating on the bulk water at different time intervals are shown. Before being irradiated, the surface temperature of the CB600 is slightly lower compared to the surroundings, making possible the absorption of energy from the environment, resulting, as will be shown later to a relatively high evaporation rate in the dark field.<sup>[55]</sup> Figure 4d shows the temperature profile of the sample and of the bulk water and background environment extracted by the IR imaging analysis as a function of the irradiation time. It can be seen that the sample's temperature increases rapidly the first 200 s up to ≈23.0 °C, while after 1 h a temperature of ≈270 °C is reached on the surface of the sample, about 6.3 °C higher than the bulk water at the same time.

One key factor to assess the viability of a material for water harvesting is the solar evaporation rate (SER), which is directly related to the amount of purified water collected through the material via steam generation and subsequent condensation. To determine SER, the mass change of the bulk water, in the presence of the CB600, was recorded as a function of time for a fixed illuminated surface area of the sample (Figure 5a). As shown, the reduction of water mass due to evaporation through the CB600, under dark and one sun irradiation, is linear over time, but upon irradiation the reduction rate is significantly higher. The calculated evaporation rate after reaching the steady-state condition is  $1.82 \text{ kg m}^{-2} \text{ h}^{-1}$ , 6.3 times higher than the rate of the bulk water and 2.8 times higher than the evaporation rate of the CB600 under dark (Figure 5b). Based on these values, and after subtracting the evaporation rate in dark conditions, the SER of the CB600 reaches  $1.17 \text{ kg m}^{-2} \text{ h}^{-1}$ , with solar-to-vapor conversion efficiency of 80% (details of heat loss analysis in Section SI10, Supporting Information).

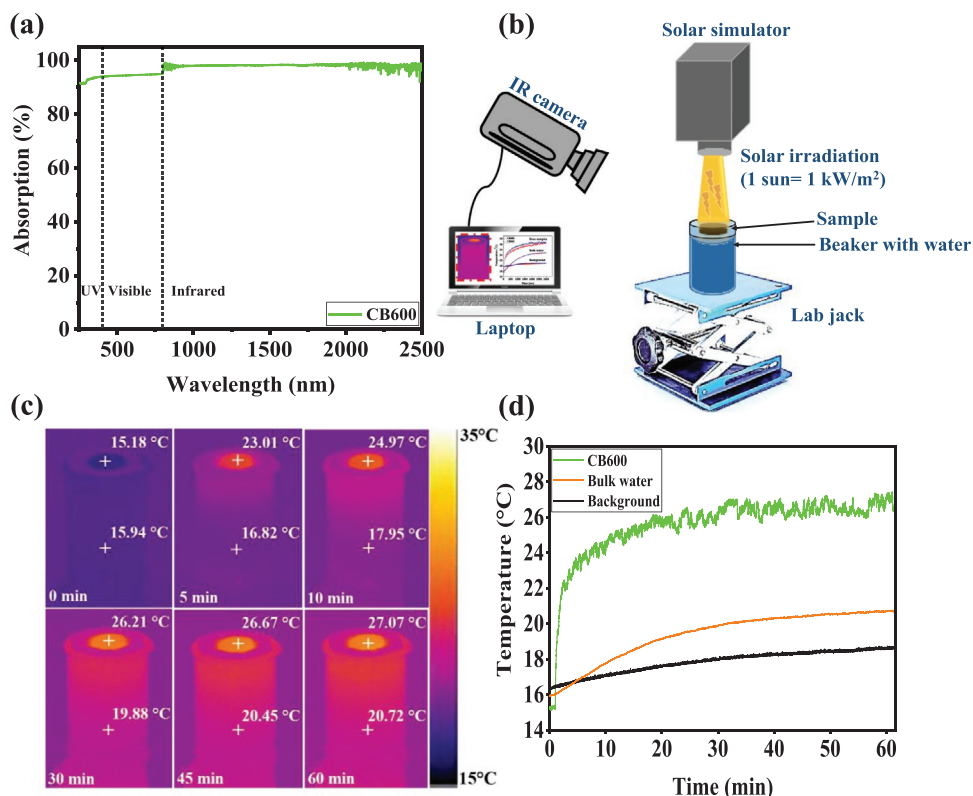


**Figure 4.** a) Representative UV–vis–NIR absorption spectra of the CB600. b) Schematic illustration of the experimental setup for the infrared-images acquisition of the CBs in contact with water under one sun illumination. c) The acquired infrared-images of the CB600 irradiated under one sun for 0, 5, 10, 30, 45, and 60 min. d) Dependence of the temperature of the CB600, bulk water, and background to the time of irradiation.

Before testing the performance of the CB600 in photo-thermal desalination, its self-desalting ability is tested. Specifically, 0.26 g of solid NaCl was put on its surface while floating on synthetic seawater (3.5 wt%). As shown in Figure S14 in the Supporting Information, the salt gradually dissolved over 4 h in the bulk water both under dark and solar irradiation of 1 Sun. This can be attributed to the abundant hierarchical pores of the CB600 which allows for capillarity-driven water uptake, serving as continuous water transport channels through which salt can move from the upper surface to the underneath water.<sup>[16,19]</sup>

For the seawater desalination test, a glass-made specific condensation chamber comprising a beaker, dome, and glass vial was used, as shown in Figure 5c. The quantity of the water collected from the condensation of the vapors generated via solar evaporation of synthetic seawater with a rate of  $\approx 0.65 \text{ L m}^{-2} \text{ h}^{-1}$  reveals that the concentration of the five primary ions originally presents in seawater has been significantly decreased by approximately three to four orders of magnitude, with ions removal efficiency higher than 99.99% as compared to the saline water (Figure 5d). In fact, after the desalination experiment the ions concentration of  $\text{Na}^+$ ,  $\text{Mg}^{2+}$ ,  $\text{K}^+$ ,  $\text{Ca}^{2+}$ , and  $\text{Sr}^+$  in the collected water are 8.70, 0.90, 0.75, 0.45, and 0  $\text{mg L}^{-1}$ , respectively, lower than the values set by WHO (World Health Organization) for the drinking water such as (100, 50, 10, and 3  $\text{mg L}^{-1}$ ).<sup>[56,57]</sup> These values not only meet the WHO drinking water standards but also are lower than that of the water recovered after treatment using

the current state-of-the-art thermal distillation ( $1\text{--}50 \text{ mg L}^{-1}$ ) and membrane-based seawater desalination processes ( $10\text{--}500 \text{ mg L}^{-1}$ ).<sup>[58]</sup>

### 3. Conclusion

To conclude, the intrinsic light absorption ability, sufficient thermal conductivity, and enhanced surface wettability together with the interlinked microchannels and hierarchical porous structure of the CB600 lead to its improved light-harvesting and steam-generation ability. Although bone based biowaste shows great inhomogeneities in terms of composition and structure that may affect the overall performance, this study turns the attention toward the potential utilization of this unique porous system in water harvesting applications after the appropriate thermal treatment. Considering the low-cost and high surplus of bone waste, a CB-based solar steam generation and desalination device specifically designed in order to host and join multiple pieces of the active material can work as an appropriate tool to mitigate the water shortage problem. Efficient use of bone waste into a valuable photothermal device, tackles various issues raised in the United Nation's sustainable development goals (SDGs). In particular, the present study not only deals with the prevention of water scarcity issues contributing to SDG6 (clean water for all) but also presents an innovative and sustainable way for food waste management contributing to the SDG12.

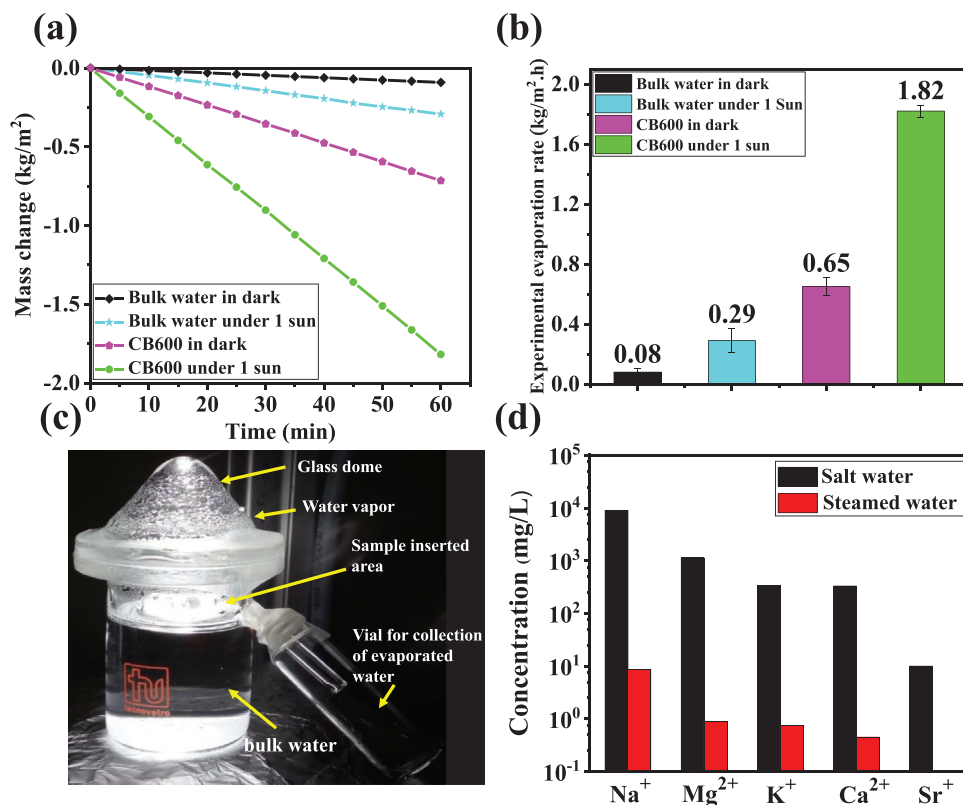


**Figure 5.** a) Cumulative mass change of pure water without and with the presence of the CB600, under dark and one sun illumination as a function of time. b) Corresponding water evaporation rate of pure water and the CB600 in dark and one sun illumination. c) Glass condensation chamber used for seawater desalination. The sample was irradiated under one sun for 12 h. d) The concentration of different metal ions in synthetic seawater (3.5 wt%) before and after treatment.

## 4. Experimental Section

**Materials:** Cattle bone waste (i.e., femur), a male animal of 6 months old with category V (Osso di Vitello) was collected from a local meat market in Genoa, Italy. Synthetic sea-salt (NutriSelect Basic, S9883), to prepare artificial seawater, was purchased from Sigma-Aldrich. Deionized (DI) water was used for all the experiments.

**Materials Preparation:** The cattle bone waste was boiled in water for 15 min to remove meat residues and other organic impurities (pristine bone). Subsequently, the pristine bone was stored in a freezer at  $-18^{\circ}\text{C}$  in an airtight plastic bag until further use. For the CB preparation, the pristine bones were sectioned transversally, perpendicular to the bone axis by a hacksaw into thin slices. Sandpaper was used to optimize the dimensions of the slices (thickness: 4.0 mm, diameter:  $\approx 9.5$ – $10.0$  mm). These bone pieces were then directly carbonized in a tube furnace (three zone split furnace: PSC 12/-/600H, Lenton, UK) under nitrogen ( $\text{N}_2$ ) atmosphere (gas flow:  $5\text{ cm}^3\text{ min}^{-1}$ ) at three different temperatures (400, 600, and  $800^{\circ}\text{C}$ ) for 1 h, with a heating rate of  $5^{\circ}\text{C min}^{-1}$ . After carbonization, the CBs were cooled down naturally under  $\text{N}_2$  atmosphere until the room temperature is reached.

**Characterization:** The morphology of the CBs was studied by SEM (JEOL JSM-6490LA) operating at an acceleration voltage of 10 kV. SEM images were acquired at three different positions of the slices, namely external, internal and cross-section surface, as shown in Figure S1 in the Supporting Information. All samples were coated with the gold layer of 10 nm using the high-resolution sputter coater Cressington 208HR (Cressington Scientific Instrument Ltd., UK). The thermal decomposition profiles were obtained through TGA using a Q500 analyzer (TA instrument, USA, samples placed in platinum pans, heating rate:  $10^{\circ}\text{C min}^{-1}$ , range: 30– $800^{\circ}\text{C}$ ) in  $\text{N}_2$  atmosphere (flow rate:  $50\text{ mL min}^{-1}$ ). The functional groups in the bone samples were

determined using a single-reflection attenuated total reflection (ATR) accessory (MIRacle ATR, PIKE Technologies) coupled to an FTIR (Vertex 70v FT-IR, Bruker). All the spectra presented were the average of 128 repetitive scans in the range  $4000$ – $600\text{ cm}^{-1}$  with a resolution of  $4\text{ cm}^{-1}$ , using the diamond crystal. Raman measurements were carried out using a Renishaw InVia micro-Raman spectrometer with a  $\times 50$  objective (numerical aperture of 0.75), an excitation wavelength of 514 nm line of an  $\text{Ar}^+$  laser, and an incident power less than 1 mW. XRD analysis was performed at ambient conditions using a PANalytical Empyrean X-ray diffractometer, equipped with a 1.8 kW  $\text{Cu K}\alpha$  ceramic X-ray tube and a PIXcel<sup>3D</sup>  $2 \times 2$  area detector, operating at 45 kV and 40 mA. Before measurements, the samples were ground to a fine powder and placed on a zero diffraction silica wafer. The optical absorption spectra were recorded in the range of 250–2500 nm by UV–vis–NIR spectrophotometer (Cary 5000) with the zero-baseline correction. Thermal images and surface temperature fluctuations were recorded using an IR-camera FLIR X6580sc and analyzed by FLIR ResearchIR software. For this, a glass beaker of 5 mL volume was used and the samples were placed in PS foam ring to permit their floating and at the same time to prevent the evaporation from the space between the sample and beaker walls. To study the interaction between the CBs with water, DSC (Discovery DSC 250 TA instruments) analysis was performed as described in Section S16 in the Supporting Information. The WCA was measured using the Dataphysics OCAH 200 contact angle goniometer at ambient conditions. The volume of a water droplet was  $3\text{ }\mu\text{L}$ . For each sample, WCAs at five different positions were recorded and the average value is calculated. The porosity and pore size distribution in the macroscopic range of the CBs were evaluated using MIP (ThermoFisher Scientific). To determine the pore size distribution, measurements were done using both low-pressure (Pascal 140 Evo) and high-pressure (Pascal 240 Evo) modules



with a standard dilatometer. Details are presented in Section S13 in the Supporting Information. To evaluate the porosity, the skeletal density of the samples was measured by helium pycnometry (Pycnomatic Evo, Thermo Fisher Scientific) equipped with a 4 cm<sup>3</sup> chamber, at 20 °C, as described in Section S13 in the Supporting Information. Through-plane thermal conductivity of the CBs was measured using a modified transient-plane source technique on a thermal conductivity analyzer (C-Therm Technologies, TCi) following the ASTM D7984 test method. BET and Barrette–Joynere–Halenda (BJH) analyses were conducted to get the specific surface area and pore size distribution of the CBs in the micro and mesoporous range. For this objective, the samples were first degassed at 150 °C under vacuum for 180 min to eliminate the partially adsorbed water molecules. Subsequently, nitrogen physisorption measurements were performed by using the gas sorption analyzer Autosorb-iQ (Quantachrome Instruments) at a temperature of 77 K. The specific surface area of the samples were measured with the assistance of a multipoint BET model by taking into account 20 uniformly spaced points in the  $P/P_0$  range from 0.05 to 0.3. The relative pressure ( $P/P_0$ ) is the pressure of the adsorbate ( $P$ ) divided by its saturation pressure ( $P_0$ ). The pore size distribution was determined from the desorption isotherms (range  $0.35 < P/P_0 < 1$ ) with the assistance of the BJH model, considering 13 points.

**Solar-Steam Generation and Desalination:** The experiments were typically conducted at ambient conditions (temperature  $17 \pm 1$  °C and relative humidity of  $50\% \pm 1\%$ ). The CBs were supported by a PS foam ring (4 mm thickness) to make them float on the water surface, covering the whole area of the glass beaker while making contact with the bulk water from the bottom side of the sample. The solar simulator used was a ScienceTech SLB-150B (Class BAA) with an air mass (AM) filter (AM1.5G) and calibrated by an Oriel reference solar cell and meter (91150V). The SER was calculated using the surface area of the sample, excluding the surface area of the PS foam ring. The mass change of water due to evaporation under one-sun illumination (corresponding to  $1 \text{ kW m}^{-2}$ ) for 60 min was measured in real-time using an analytical balance (Kern, 0.01 mg accuracy). The final evaporation rates ( $\dot{m}$  in  $\text{kg m}^{-2} \text{ h}^{-1}$ ) were obtained upon the subtraction of the evaporation rate of the samples in the dark.<sup>[55]</sup>

The solar-to-vapor conversion efficiency ( $\eta$ ) was calculated according to Equation (1)<sup>[55]</sup>

$$\eta = \frac{\dot{m}(L_v + Q)}{q_{in}} \quad (1)$$

where  $\dot{m}$  is the SER improvement under illumination (the difference between the evaporation rates with and without light as calculated above),  $L_v$  is the latent heat of water phase change enthalpy ( $\text{J kg}^{-1}$ ),  $Q$  is the sensible heat of water ( $\text{J kg}^{-1}$ ), and  $q_{in}$  is the power of solar illumination ( $1 \text{ kW m}^{-2}$ ).  $L_v$  depends on the temperature at which water evaporation occurs and ranges from  $2256.4 \text{ kJ kg}^{-1}$  at  $100$  °C to  $2453.5 \text{ kJ kg}^{-1}$  at  $20$  °C, while  $Q$  is calculated by multiplying the specific heat capacity of water ( $4.18 \text{ kJ kg}^{-1} \text{ °C}^{-1}$ ) with the temperature difference ( $\Delta T$ ) of the bulk water during the evaporation process.

Desalination experiments were conducted in a custom-made glass condensation chamber. To do so, 3.5 wt% of synthetic sea-salt was added to DI water to prepare seawater. Then, the CB with the support of the PS foam ring was placed on the prepared seawater for 12 h in the glass chamber under one sun illumination. The distillate after its condensation was collected and the concentrations of primary ions ( $\text{Na}^+$ ,  $\text{K}^+$ ,  $\text{Ca}^{2+}$ ,  $\text{Mg}^{2+}$ , and  $\text{Sr}^{2+}$ ) before and in the distillate were analyzed by an inductively coupled plasma (ICP) optical emission spectrometer (iCAP 6300, ThermoFisher-Scientific).

## Supporting Information

Supporting Information is available from the Wiley Online Library or from the author.

## Acknowledgements

The authors would like to thank S.-L. Loo for useful discussions, L. Marini for Thermal analyses, G. Mancini for the MIP studies, L. Marasco for helping in the carbonization process, R. Kaiukov for XRD analyses, L. Pasquale for BET analyses, G. La Rosa for UV–vis–NIR spectroscopy, and F. Drago for ICP analyses.

## Conflict of Interest

The authors declare no conflict of interest.

## Data Availability Statement

Research data are not shared.

## Keywords

biomass, hydroxyapatite, light-harvesting, photothermal evaporation, water management

Received: February 4, 2021

Revised: May 3, 2021

Published online:

- [1] P. Messerli, *Global Sustainable Dev. Rep.* **2019**, *102*, 155.
- [2] M. Elimelech, W. A. Phillip, *Science* **2011**, *333*, 712.
- [3] C. Zhang, H.-Q. Liang, Z.-K. Xu, Z. Wang, *Adv. Sci.* **2019**, *6*, 1900883.
- [4] P. J. J. Alvarez, C. K. Chan, M. Elimelech, N. J. Halas, D. Villagrán, *Nat. Nanotechnol.* **2018**, *13*, 634.
- [5] L. Zhou, Y. Tan, D. Ji, B. Zhu, P. Zhang, J. Xu, Q. Gan, Z. Yu, J. Zhu, *Sci. Adv.* **2016**, *2*, e1501227.
- [6] J. Wang, Y. Li, L. Deng, N. Wei, Y. Weng, S. Dong, D. Qi, J. Qiu, X. Chen, T. Wu, *Adv. Mater.* **2017**, *29*, 1603730.
- [7] H. Ghasemi, G. Ni, A. M. Marconnet, J. Loomis, S. Yerci, N. Miljkovic, G. Chen, *Nat. Commun.* **2014**, *5*, 4449.
- [8] S.-L. Loo, L. Vásquez, U. C. Paul, L. Campagnolo, A. Athanassiou, D. Fragouli, *ACS Appl. Mater. Interfaces* **2020**, *12*, 10307.
- [9] P. Sun, W. Zhang, I. Zada, Y. Zhang, J. Gu, Q. Liu, H. Su, D. Pantelić, B. Jelenković, D. Zhang, *ACS Appl. Mater. Interfaces* **2020**, *12*, 2171.
- [10] Y. Yang, R. Zhao, T. Zhang, K. Zhao, P. Xiao, Y. Ma, P. M. Ajayan, G. Shi, Y. Chen, *ACS Nano* **2018**, *12*, 829.
- [11] P. Mu, Z. Zhang, W. Bai, J. He, H. Sun, Z. Zhu, W. Liang, A. Li, *Adv. Energy Mater.* **2019**, *9*, 1802158.
- [12] N. Xu, X. Hu, W. Xu, X. Li, L. Zhou, S. Zhu, J. Zhu, *Adv. Mater.* **2017**, *29*, 1606762.
- [13] Y. Long, S. Huang, H. Yi, J. Chen, J. Wu, Q. Liao, H. Liang, H. Cui, S. Ruan, Y. J. Zeng, *J. Mater. Chem. A* **2019**, *7*, 26911.
- [14] X. Zhou, J. Li, C. Liu, F. Wang, H. Chen, C. Zhao, H. Sun, Z. Zhu, *Int. J. Energy Res.* **2020**, *44*, 9213.
- [15] Y. Lu, X. Wang, D. Fan, H. Yang, H. Xu, H. Min, X. Yang, *Sustainable Mater. Technol.* **2020**, *25*, e00180.
- [16] C. Wang, J. Wang, Z. Li, K. Xu, T. Lei, W. Wang, *J. Mater. Chem. A* **2020**, *8*, 9528.
- [17] M. Zhu, J. Yu, C. Ma, C. Zhang, D. Wu, H. Zhu, *Sol. Energy Mater. Sol. Cells* **2019**, *191*, 83.
- [18] J. Li, X. Zhou, J. Zhang, C. Liu, F. Wang, Y. Zhao, H. Sun, Z. Zhu, W. Liang, A. Li, *ACS Appl. Mater. Interfaces* **2020**, *3*, 3024.

- [19] Y. Guo, H. Lu, F. Zhao, X. Zhou, W. Shi, G. Yu, *Adv. Mater.* **2020**, *32*, 1907061.
- [20] Y. Zhang, S. K. Ravi, S. C. Tan, *Nano Energy* **2019**, *65*, 104006.
- [21] Y. Zhang, S. K. Ravi, J. V. Vaghasiya, S. C. Tan, *iScience* **2018**, *3*, 31.
- [22] J. Li, X. Zhou, G. Chen, F. Wang, J. Mao, Y. Long, H. Sun, Z. Zhu, W. Liang, A. Li, *Sol. Energy Mater. Sol. Cells* **2021**, *222*, 110941.
- [23] I. Ibrahim, V. Bhoopal, D. H. Seo, M. Afsari, H. K. Shon, L. D. Tijing, *Mater. Today Energy* **2021**, *21*, 100716.
- [24] D. A. Teigiserova, L. Hamelin, M. Thomsen, *Sci. Total Environ.* **2020**, *706*, 136033.
- [25] J. Niu, R. Shao, M. Liu, Y. Zan, M. Dou, J. Liu, Z. Zhang, Y. Huang, F. Wang, *Adv. Funct. Mater.* **2019**, *29*, 1905095.
- [26] Y. Yao, F. Wu, *Nano Energy* **2015**, *17*, 91.
- [27] J. Niu, R. Shao, M. Liu, J. Liang, Z. Zhang, M. Dou, Y. Huang, F. Wang, *Energy Storage Mater.* **2018**, *12*, 145.
- [28] B. Shan, Y. Cui, W. Liu, Y. Zhang, S. Liu, H. Wang, L. Sun, Z. Wang, R. Wu, A. C. S. Sustain, *Chem. Eng.* **2018**, *6*, 14989.
- [29] R. Wang, K. Wang, Z. Wang, H. Song, H. Wang, S. Ji, *J. Power Sources* **2015**, *297*, 295.
- [30] M. K. Shahid, J. Y. Kim, Y. G. Choi, *Groundwater Sustainable Dev.* **2019**, *8*, 324.
- [31] U. E. Pazzaglia, T. Congiu, M. Raspanti, F. Ranchetti, D. Quacci, *Clin. Orthop. Relat. Res.* **2009**, *467*, 2446.
- [32] M. Figueiredo, A. Fernando, G. Martins, J. Freitas, F. Judas, H. Figueiredo, *Ceram. Int.* **2010**, *36*, 2383.
- [33] M. Krzesińska, J. Majewska, *J. Anal. Appl. Pyrolysis* **2015**, *116*, 202.
- [34] M. Younesi, S. Javadpour, M. E. Bahrololoom, *J. Mater. Eng. Perform.* **2011**, *20*, 1484.
- [35] C. Y. Ooi, M. Hamdi, S. Ramesh, *Ceram. Int.* **2007**, *33*, 1171.
- [36] C. K. Rojas-Mayorga, A. Bonilla-Petriciolet, I. A. Aguayo-Villarreal, V. Hernández-Montoya, M. R. Moreno-Virgen, R. Tovar-Gómez, M. A. Montes-Morán, *J. Anal. Appl. Pyrolysis* **2013**, *104*, 10.
- [37] J. O. Akindoyo, M. D. H. Beg, S. Ghazali, E. O. Akindoyo, N. Jeyaratnam, *IOP Conf. Ser. Mater. Sci. Eng.* **2017**, *203*, 012003.
- [38] J. O. Akindoyo, S. Ghazali, M. D. H. Beg, N. Jeyaratnam, *Chem. Eng. Technol.* **2019**, *42*, 1805.
- [39] R. Murugan, K. P. Rao, T. S. S. Kumar, *Bull. Mater. Sci.* **2003**, *26*, 523.
- [40] Q. Wang, W. Li, R. Liu, K. Zhang, H. Zhang, S. Fan, Z. Wang, *Int. J. Legal Med.* **2019**, *133*, 269.
- [41] P. Yu, D. Damiran, *Spectrochim. Acta, Part A* **2011**, *79*, 51.
- [42] A. Boskey, N. P. Camacho, *Biomaterials* **2007**, *28*, 2465.
- [43] M. P. M. Marques, D. Gonçalves, A. P. Mamede, T. Coutinho, E. Cunha, W. Kockelmann, S. F. Parker, L. A. E. Batista de Carvalho, *Sci. Rep.* **2021**, *11*, 1361.
- [44] J. Niu, R. Shao, J. Liang, M. Dou, Z. Li, Y. Huang, F. Wang, *Nano Energy* **2019**, *36*, 322.
- [45] M. Zahid, A. E. Del Río Castillo, S. B. Thorat, J. K. Panda, F. Bonaccorso, A. Athanassiou, *Compos. Sci. Technol.* **2020**, *200*, 108461.
- [46] F. Liu, R. Wang, Y. Cheng, X. Jiang, Q. Zhang, M. Zhu, *Mater. Sci. Eng., C* **2013**, *33*, 4994.
- [47] J. Liu, H.-B. Zhang, R. Sun, Y. Liu, Z. Liu, A. Zhou, Z.-Z. Yu, *Adv. Mater.* **2017**, *29*, 1702367.
- [48] L. Zahid, H. Li, Q. Song, K. Li, J. Lu, W. Li, S. V. Mikhlovsky, S. Cao, *Surf. Rev. Lett.* **2014**, *21*, 1450016.
- [49] Z. H. Ping, Q. T. Nguyen, S. M. Chen, J. Q. Zhou, Y. D. Ding, *Polymer* **2001**, *42*, 8461.
- [50] M. U. S. Jhon, J. D. Andrade, *J. Biomed. Mater. Res.* **1973**, *7*, 509.
- [51] Y. Zhang, T. Xiong, D. K. Nandakumar, S. C. Tan, *Adv. Sci.* **2020**, *7*, 1903478.
- [52] F. Zhao, Y. Guo, X. Zhou, W. Shi, G. Yu, *Nat. Rev. Mater.* **2020**, *5*, 388.
- [53] Z. Zhang, Y. Wang, P. A. Stensby Hansen, K. Du, K. R. Gustavsen, G. Liu, F. Karlsen, O. Nilsen, C. Xue, K. Wang, *Nano Energy* **2019**, *65*, 103992.
- [54] G. Xue, K. Liu, Q. Chen, P. Yang, J. Li, T. Ding, J. Duan, B. Qi, J. Zhou, *ACS Appl. Mater. Interfaces* **2017**, *9*, 15052.
- [55] C. Shen, Y. Zhu, X. Xiao, X. Xu, X. Chen, G. Xu, *ACS Appl. Mater. Interfaces* **2020**, *12*, 35142.
- [56] L. Yang, G. Chen, N. Zhang, Y. Xu, X. Xu, *ACS Sustainable Chem. Eng.* **2019**, *7*, 19311.
- [57] M. Zhu, A. Xia, Q. Feng, X. Wu, C. Zhang, D. Wu, H. Zhu, *Energy Technol.* **2020**, *8*, 1901215.
- [58] F. Zhao, X. Zhou, Y. Shi, X. Qian, M. Alexander, X. Zhao, S. Mendez, R. Yang, L. Qu, G. Yu, *Nat. Nanotechnol.* **2018**, *13*, 489.